Journal of Alloys and Compounds 509 (2011) 1011–1019

Contents lists available at ScienceDirect

Journal of Alloys and Compounds

journal homepage: www.elsevier.com/locate/jallcom

Approach of the spark plasma sintering mechanism in $Zr_{57}Cu_{20}Al_{10}Ni_8Ti_5$ metallic glass

Sophie Nowak[a], Loïc Perrière[a,*], Lucas Dembinski[b], Sandrine Tusseau-Nenez[a], Yannick Champion[a]

[a] ICMPE, CNRS UMR 7182, 2-8 rue Henri Dunant, 94320 Thiais, France
[b] LERMPS, Université de Technologie de Belfort-Montbéliard, 90010 Belfort, France

ARTICLE INFO

Article history:
Received 8 July 2010
Received in revised form 23 August 2010
Accepted 6 September 2010
Available online 25 October 2010

Keywords:
Metallic glass
Spark plasma sintering
Sintering process
Mechanical behaviour

ABSTRACT

Spark plasma sintering (SPS) was used to sinter gas-atomized $Zr_{57}Cu_{20}Al_{10}Ni_8Ti_5$ amorphous powder. Systematic analyses were performed to study particle size and annealing time effects on the parts structure and properties. Partial devitrification and particles welding were observed and correlated to particle size and thermal conditions. Mechanical testing, through compression and micro-hardness, reveals that the sintered parts show strength similar to a quenched bulk metallic glass and damaging before failure. However, the pulsed current input does not seem the most relevant way to sinter amorphous powders: during the sintering initial stages (when necks are small), excessive over-heating is generated in the vicinity of particles necks, and is responsible for partial devitrification; further current input at large necks leads to complete densification. Effects of the stress, the thermo- and electro-transports on the sintering are evaluated to provide a better understanding of the SPS mechanisms of densification of metallic glasses.

1. Introduction

Bulk metallic glasses (BMG) are among the most recent innovative metallic materials [1] in particular for their remarkable mechanical properties attractive for various applications [2,3]. BMG exhibit behaviours close to those of oxide glasses. In particular, they present a glass transition temperature, T_g. At $T > T_g$, the deformation is viscous-like, and occurs at low stress. At $T < T_g$, BMG possess high strength (close to the theoretical $\sigma_{max} \approx E/20$) and no ductility. BMG undergo an average 2% elastic deformation and then possess large resilience (σ^2_{max}/E) owing to Young modulus similar to those of their crystalline counterparts. Formation of metallic glasses is kinetically (rather than thermodynamically) controlled and obeys empirical rules first stated by Inoue [4]. At present, some amorphous phases have been discovered (with major element Zr, Ti, Cu, Pd, Mg, Pt, Ca, Fe, Ni, Co and rare earths) covering reasonable domains of properties (mechanical, magnetic, exhibiting remarkable resistance to corrosion, wear and low friction stress) [5–7]. Nevertheless, the bulk forms are still limited in shapes and dimensions and are generally very complex in composition [8]. In contrast, a wide variety of glasses which might be of interest are obtained into ribbon forms (few tens of microns) only by melt spinning techniques (quenching rate around 10^6 K s^{-1}).

Powder metallurgy is the relevant alternative process in metallurgical engineering to produce large size specimens with controlled size and shape. Main benefit for amorphous is that powder particles of few micrometers in size should be fabricated from any glass system, even those having low glass forming ability (GFA). Amorphous powders were successfully produced since the late 70s by atomization techniques (water and now gas) with an estimated quenching rate of 10^6 K s^{-1} [9]. Since then, production of bulk glasses using conventional sintering assisted by pressure techniques, such as hot extrusion [10] or hot pressing [11], has been studied. These processes have opened promising perspectives for BMG though they have to face drastic experimental problems. Easy and near full densification is obtained under reasonable pressure above T_g, but a long time above this temperature is necessary to reach full consolidation (particles welding). This annealing thoroughly leads to high rate of devitrification in the material [12].

Along with the development of spark plasma sintering (SPS), the processing of metallic glass (MG) powders has regained in interest. The main asset of this technique is to provide extremely rapid heating, and thus likely limit the crystallisation of MGs. Moreover, many experiments on various metallic powders showed that oxide is broken at the particles surface during current heating which significantly improves the sintering [13]. Consolidation with SPS of atomized MG powders has thus been obtained for Fe-based alloys, with good magnetic properties [14,15], for Cu- and Ni-based alloys with high hardness and strength [16,17]. The technique has also

* Corresponding author. Tel.: +33 0 1 56 70 30 38.
E-mail address: perriere@icmpe.cnrs.fr (L. Perrière).

0925-8388/$ – see front matter © 2010 Published by Elsevier B.V.
doi:10.1016/j.jallcom.2010.09.158

shown further perspective for the development of architectured materials with the fabrication of *in situ* composites (devitrification in powder fabrication [18] or during SPS [19]), *ex situ* composites by powder mixing [20,21], or dual amorphous materials [22]. These new architectured materials exhibit interesting behaviours such as improved ductility and damage resistance.

This paper reports on an analysis of SPS consolidation of $Zr_{57}Cu_{20}Al_{10}Ni_8Ti_5$ metallic glass produced by gas atomization [23]. This MG was selected because it possesses a high GFA [24]. The bulk monolithic form was intensively studied towards its mechanical behaviour, and is then a relevant reference for comparison with sintered parts [25,26]. Our study first aims to produce bulk SPSed specimens with ultimate strength in the range of the BMG's one. Moreover, systematic thermal, structural and mechanical analysis of SPS consolidated powders with various grain sizes have been performed to shed light on SPS specific mechanisms of densification and consolidation. Post mortem analysis of specimens, which reveals non systematic partial devitrification (see for example differences in [19,22]), points out, with clear evidences, some physical events that are non observable in crystalline solids. From these investigations, we aim to approach the specific mechanisms of sintering through SPS of metallic glasses and, more generally, metallic alloys.

2. Experimental procedure

2.1. Materials synthesis

Gas atomization necessitates at least 1 kg of the $Zr_{57}Cu_{20}Al_{10}Ni_8Ti_5$ alloy, initially prepared with high purity metals (>99.9% GoodFellow and Cerac). Ten distinct ingots were melted using high frequency induction melting in water cooled copper crucible and then re-melted in the oven on top of the atomizer. A stream of the molten alloy then flows through the nozzle at the bottom of the crucible under pressurised argon gas (2 bars) and is fragmented in the chamber at the nozzle exit. The as-produced alloy droplets are then quenched in the atomizer and collected at the bottom of the chamber.

Atomized powder was sorted out by mechanical sieving before sintering stage. Details of powders sets are reported in Table 1. Sintering was carried out in a Syntex SPS-515S (Syntex, Japan), using WC/Co die and punches supplied by Syntex. The temperature of the sintering plateau of 663 K (controlled by a K-type thermocouple inserted into the die) is just above T_g, where homogeneous flow of the alloy is expected.

For the MG of interest, $Zr_{57}Cu_{20}Al_{10}Ni_8Ti_5$, the sintering and densification temperature domain available is extremely narrow (about 60 K) between the glass transition temperature ($T_g \approx 660$ K) and the crystallisation temperature ($T_x \approx 720$ K). It is also emphasized that the crystallisation kinetics is dramatically increased above T_g, and that much larger crystallisation rates have to be expected when sintering temperature and time are slightly increased above T_g. A preliminary experiment (G0, see Table 1) was thus carried out to determine the optimal densification temperature, between 600 K and 683 K. Further experiments were thus carried out at 663 K, in order to maximise the densification and minimize the crystallisation of the MG.

To reach full densification, the samples (10 mm in diameter and 4.5 mm final thickness) are pressed at a loading rate of 20 kN min^{-1}–40 kN (about 500 MPa on the sample). A heating rate of 60 K min^{-1} was then applied from room temperature up to 573 K. The heating rate was slowed down to 10 K s^{-1} from 573 K to 663 K, in order to avoid temperature overshoot and thus likely crystallisation of the MG. Holding time varied from 3 to 10 min, depending on the sample (see Table 1 for details). All experiments were carried out under vacuum (7.5×10^{-2} Torr). Sample heating is resulting from Joule dissipation of pulsed electric current. The necessary electric energy is provided by high current intensity (up to 1300 Å) balanced by an appropriate voltage (up to 2 V). In the Syntex equipment, the pulsed current is periodically input following a set of 12 pulses (2 ms on–1 ms off) followed by 2 pauses (3 ms off). This means that, during the total duration of a cycle of pulses, the electric current is on for 24 ms upon the 42 ms of the whole cycle.

Quenched bulk samples were studied elsewhere [25,26], and the results have been used here for comparison with SPSed samples.

Table 1
Powder grains size and holding time used during SPS processing.

Sample	Max temperature (K)	Holding time (min)	Powder grains size
G0	773	0	No selection: $d_{average}$ = 70 μm
G1	663	3	No selection: $d_{average}$ = 70 μm
G2	663	5	No selection: $d_{average}$ = 70 μm
G3	663	5	32–63 μm
G4	663	5	63–125 μm
G5	663	10	32–63 μm
G6	663	10	63–125 μm

2.2. Characterisation

Chemical composition of the amorphous powder was controlled by ICP-OES analyses (Varian Vista AX, Varian Inc., USA) on three distinct powder sets. Thermal analysis were performed using differential scanning calorimetry (DSC Mettler-Toledo DSC822 calorimeter, Intl. Inc., Switzerland) at a heating rate of 20 K min^{-1}, for determination of glass transition, T_g, and crystallisation, T_x, temperatures as well as evaluation of devitrification amount after sintering. Systematic density measurements were performed on sintered parts using Archimedes principle (medium: propan-l), in order to verify if full densification was fulfilled. Structural characterisation, on both powder and sintered samples, were carried out by XRD measurements, with X-ray powder diffractometer in a Bragg–Brentano geometry (θ–θ) (X'Pert PRO MPD, PANalytical, The Netherlands) equipped with a high temperature furnace (TC RADIATION, MRI, Germany) connected to a turbomolecular pump (1×10^{-4}–5×10^{-5} mbar) and a fast detector (X'Celerator) based on real time multiple strip technology. Phase identifications were performed using EVA software (version 13, Bruker AXS, Germany) and JCPDS-International Centre for Diffraction Data powder Diffraction File (PDF-2, JCPDS-ICDD, USA). Energy dispersive X spectroscopy (EDX) and local observation were performed with an analytical transmission electron microscope (TEM – TECNAI-FEI F20, FEI, USA) with a field emission gun and operating at 200 kV. The thin foils were prepared by mechanical polishing and Ar^+ ion beam milling. Mechanical behaviour of the sintered samples was assessed by uni-axial compressive experiments, carried out on a 100 kN MTS-20/M system (MTS, USA) at strain rate of 5×10^{-5} s^{-1}, and Vickers micro-hardness (FM-0, Future-Tech Corp., Japan). Compression samples have been cut off into parallelepiped shape from the sintered pellets and polished for compression at room temperature. The fracture surfaces after mechanical testing were observed with a scanning electron microscope equipped with a field emission gun (LEO 1530, Zeiss, Germany).

3. Results

3.1. Assessment of MG powder preparation

Atomized powder particles are spherical (Fig. 1a) with average particle size of 70 μm. The size distribution, measured using laser diffusion technique, is near Gaussian (Fig. 1b). Except a thin oxide layer obviously present at their surface, the particles are amorphous within the detection limit of the X-ray diffraction (Fig. 1c). ICP-OES analyses (Table 2) show no pollution of the powder, except some iron and hafnium traces. DSC shows small variations of T_g and T_x measured on the atomized powder (Fig. 1d), compared to those measured for the bulk alloy (Table 3). The difference of crystallisation enthalpy between the bulk and the powder might be attributed to the thin oxide layer obviously present on the powder particles. This set of analyses assesses that cooling conditions in the atomizer are sufficient for producing glassy alloy. It is to be reminded that $Zr_{57}Cu_{20}Al_{10}Ni_8Ti_5$ has a particularly high GFA and is ordinary obtained as bulk over a thickness of 10 mm by cooling at rate of about 10 K s^{-1}. In atomization, particles size is of the order of usual ribbons thickness produced by melt spinning. The cooling rate is much likely of the order of 10^6 K s^{-1}.

3.2. SPS of MG powder

It is first interesting to notice that, according to density measurements reported in Table 3, G1–G6 are fully densified. Indeed, measured density (6.59) of the BMG and measured densities of G1–G6 concur, within the range of the error margin.

At the temperature of the plateau (die temperature of 663 K), relevance of the SPS technique for metallic glass powder processing was primarily evaluated with respect to annealing time and par-

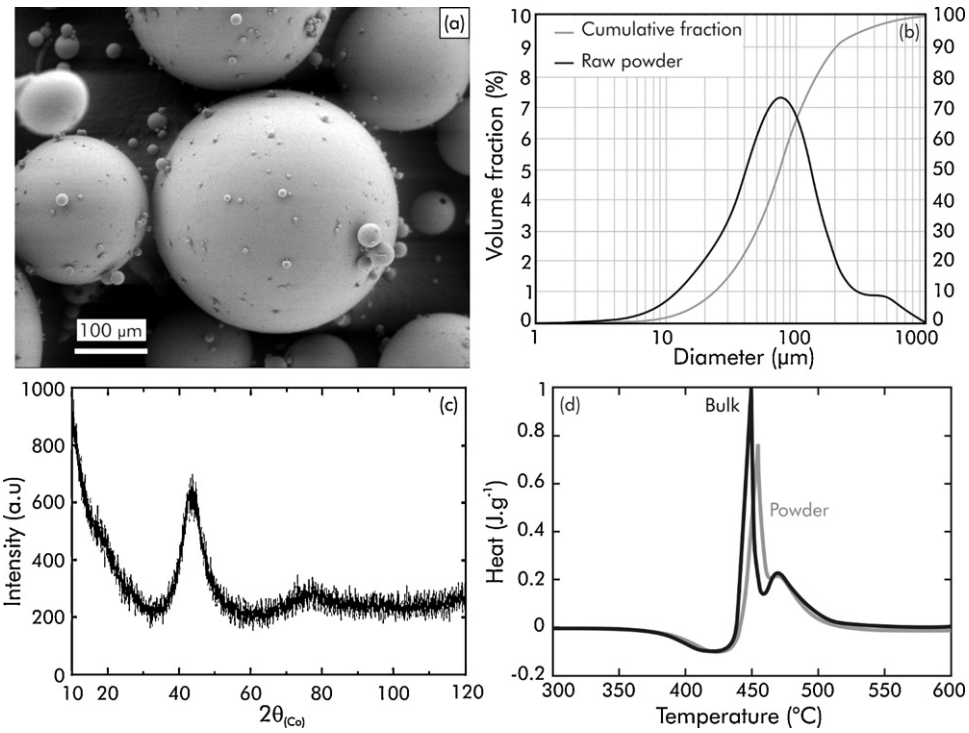

Fig. 1. (a) Scanning electron micrograph of the gas-atomized $Zr_{57}Cu_{20}Al_{10}Ni_8Ti_5$ metallic glass powder; (b) grain size analysis of the atomized amorphous powder; (c) XRD pattern obtained on raw $Zr_{57}Cu_{20}Al_{10}Ni_8Ti_5$ amorphous powder, showing the characteristic broad peaks of a disordered atomic structure; (d) comparison of the DSC analyses of $Zr_{57}Cu_{20}Al_{10}Ni_8Ti_5$ bulk metallic glass (black) and amorphous powder (grey).

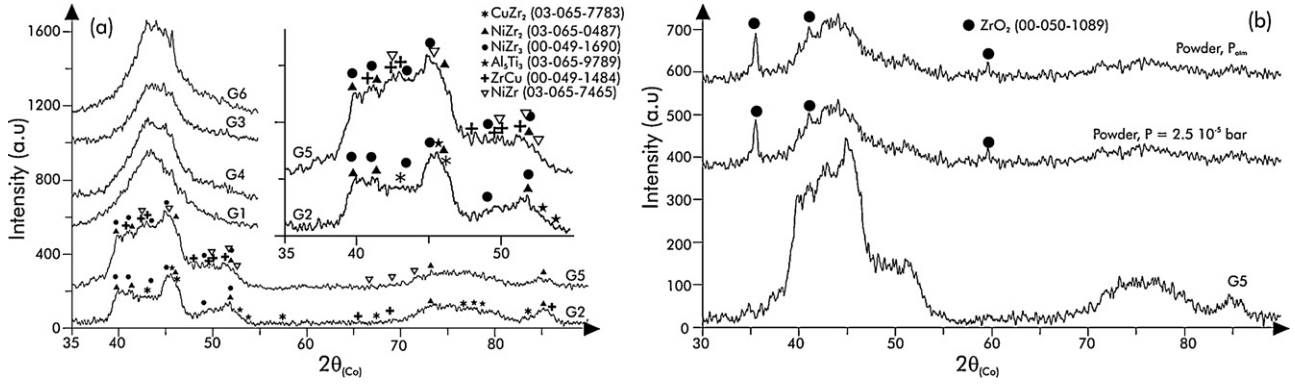

Fig. 2. (a) XRD patterns obtained on the densified samples. Inset corresponds to a zoom on small angles for G2 and G5. The PDF numbers of the patterns are mentioned in parenthesis; (b) comparison between XRD pattern obtained on G5 and HT-XRD *in situ* annealed powder. Heating rates in SPS and *in situ* HT-XRD experiments were identical. See text for further details.

ticle size (Table 1). During experiments, temperature fluctuations with time were observed. This effect is variable with specimens, not actually controlled and most likely related to some slight variations in the overall set up configuration (thermocouple position, initial green density of the loose powder). Most drastic is a temperature overshoot with a maximum of 5 K observed for G3 during about 1 min. G5 and G6 undergo an overshoot of 2.5 K for about the same period of time. X-ray diffraction patterns are displayed in Fig. 2a with intensities of crystalline reflections appearing overlaid the broad peaks of the amorphous phase. The phases produced

Table 2
Theoretical and experimental chemical compositions of the alloy. Experimental composition was determined by ICP-OES (see text for further details).

	Metal					
	Zr	Cu	Al	Ni	Ti	Traces
Theoretical mass. %	69.9	17	3.6	6.3	3.2	0
Actual mass. %	> 50	16.2 ± 0.2	3.82 ± 0.0	6.02 ± 0.0	2.9 ± 0.1	Hf, Fe

Table 3
Thermal properties and density of the $Zr_{57}Cu_{20}Al_{10}Ni_8Ti_5$ bulk metallic glass, amorphous powder and sintered samples.

Sample	Crystallisation enthalpy ($J\,g^{-1}$)	Glass transition temperature, T_g (K)	Crystallisation temperature, T_x (K)	Density
Bulk	61.9	658	722	6.59 ± 0.01
Powder	54.8	657	727	–
G1	36.8	658	721	6.57 ± 0.02
G2	23.7	653	740	6.59 ± 0.03
G3	43.5	655	718	6.60 ± 0.02
G4	51.0	655	723	6.58 ± 0.02
G5	37.4	658	718	6.61 ± 0.03
G6	45.2	653	718	6.60 ± 0.02

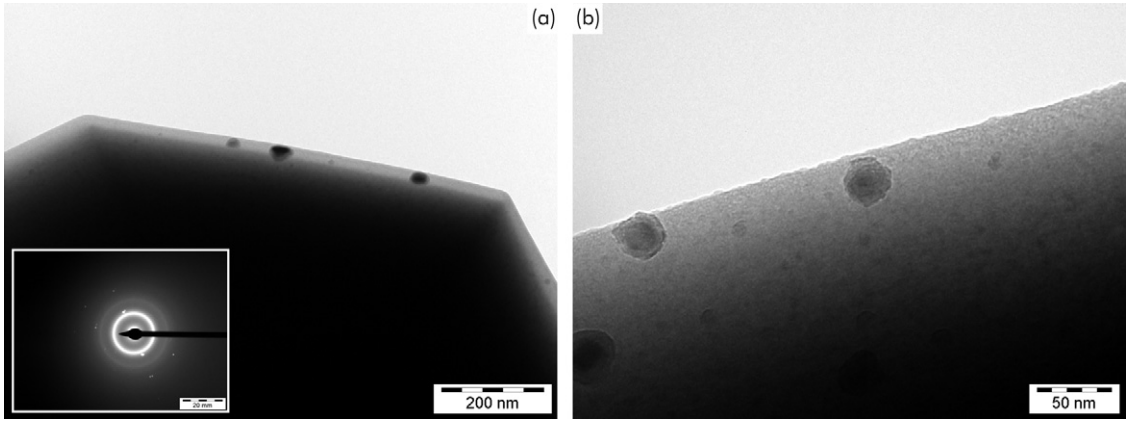

Fig. 3. TEM micrographs of a sintered sample. Nano-precipitates (<50 nm in diameter) are clearly present in the central part of the particle facet (a and b). (a) The inset shows a selected area diffraction pattern, where broad rings, characterising the glassy matrix, but also some crystalline spots, are visible.

by devitrification of the SPS samples can be identified more easily on G2 and G5 samples. These samples exhibit broad peaks, characteristic of nanocrystalline phases. For G5, the main phase is Ni_2Zr_3 metastable [27] in equilibrium with tetragonal $NiZr_2$, orthorhombic NiZr and monoclinic CuZr. Crystalline phases in G2 are orthorhombic Al_5Ti_3, metastable Ni_2Zr_3, tetragonal $NiZr_2$ and tetragonal $CuZr_2$. *In situ* XRD patterns (Fig. 2b) were performed for 10 min annealing at 663 K under atmospheric pressure and 2.5×10^{-5} bar on the loose powder and compared to G5 (partially crystallised sintered sample). Heating rate was identical to the SPS ones (see Section 2.1). Both annealed powders show evidence of oxidation with diffraction peaks corresponding to tetragonal ZrO_2 (due to oxygen vacancies under vacuum), that are not present in SPS samples (e.g. G5). The CuZr phase, which is a high temperature phase (stable above 1000 K), is observed only in the short time annealed sample (G3, G4). It was observed elsewhere that this CuZr phase appears at the first DSC peak of crystallisation (see Fig. 1d) (unpublished data). It would indicate that high temperature and less stable phases appear first at short annealing time and then disappear by reaction after further annealing to form stable phases according to the phase diagram. All sintered samples present crystallisation peaks with the largest intensities for G2 and G5. It is interesting to notice that G3, which underwent the maximum temperature overshoot, exhibits the less crystallisation along with G4. This indicates that there is no real correlation between the temperature overshoot and the rate of crystallisation, at least in these ranges of temperature and time. In contrast, larger crystallisation rate is noticeable for longer annealing times (G5 and G6). Another interesting result is that G5 exhibits a larger crystallisation rate than G6. A simple assumption would be to consider that devitrification occurs initially at particles neck where electric current density, and thus temperature (produced by Joule dissipation effect), are the largest (electric intensity scaled by small neck size at the early stage of sintering, see discussion). This assumption was qualitatively supported by transmission electron microscopy observations. In Fig. 3, the polygonal surface area is corresponding to former neck zones between particles, revealed by preferential etching during ion milling. A thin zone at the sample edge contains nanoparticles with diameter of about 20–50 nm, coming from partial devitrification. A rough estimate of the chemical composition, since particles are small and embedded in the glassy matrix, was provided by TEM EDX analysis. It is also worth noticing that a significant enrichment in copper content has been detected. This is consistent with the XRD indexed ZrCu phase. Assuming a constant devitrification amount (only temperature dependant) and an identical number of contacts for each particle for the range of particle sizes (about six for hard spheres packing), then the average volume fraction of devitrification zones, χ_c, varies with the particles size, D, following: $\chi_c \propto 1/D^3$. This means that, for a ratio of particles size of 1:2 (see, for example, G5 and G6), the difference in volume fraction of crystallites should be 1:8. This dependence of the crystallisation amount with grain size is confirmed by DSC analysis (Fig. 4), where variation in crystallisation enthalpies are estimated from peaks integral breadth (Table 3) for samples having various particles sizes and for the same annealing time (5 min) in SPS. It must be noticed that only the first peak of crystallisation decreases in intensity. In addition, the curves profile around T_g is slightly modified, which would indicate that free volume content changes (or local ordering changes) during SPS treatment. Crystallisation enthalpy decreases logically from G4 to G3, which has the smaller particles size (hence larger devitrification probability). G2 shows the largest enthalpy variation (the first crystallisation peak is barely visible) with respect to the powder, though its average particle size is the largest (70 μm). This result must be related to the particle size distribution which is the widest for G2 (where no sieving was performed) and resulting in an increase of the average number of contact points and a greater devitrification rate consequently.

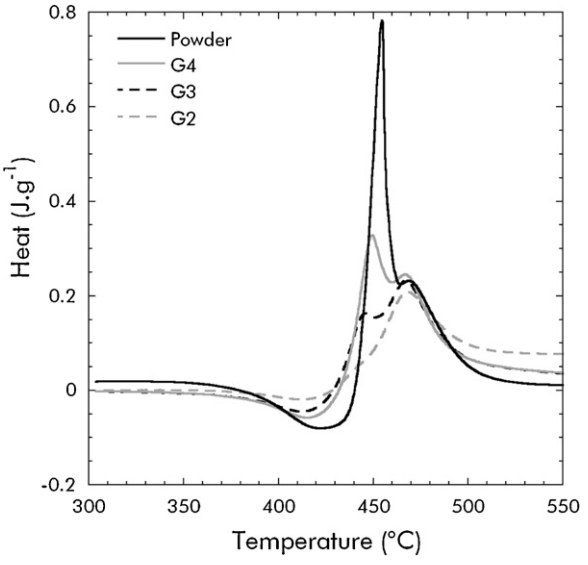

Fig. 4. DSC scans of $Zr_{57}Cu_{20}Al_{10}Ni_8Ti_5$ amorphous powder and G2–G4 sintered samples.

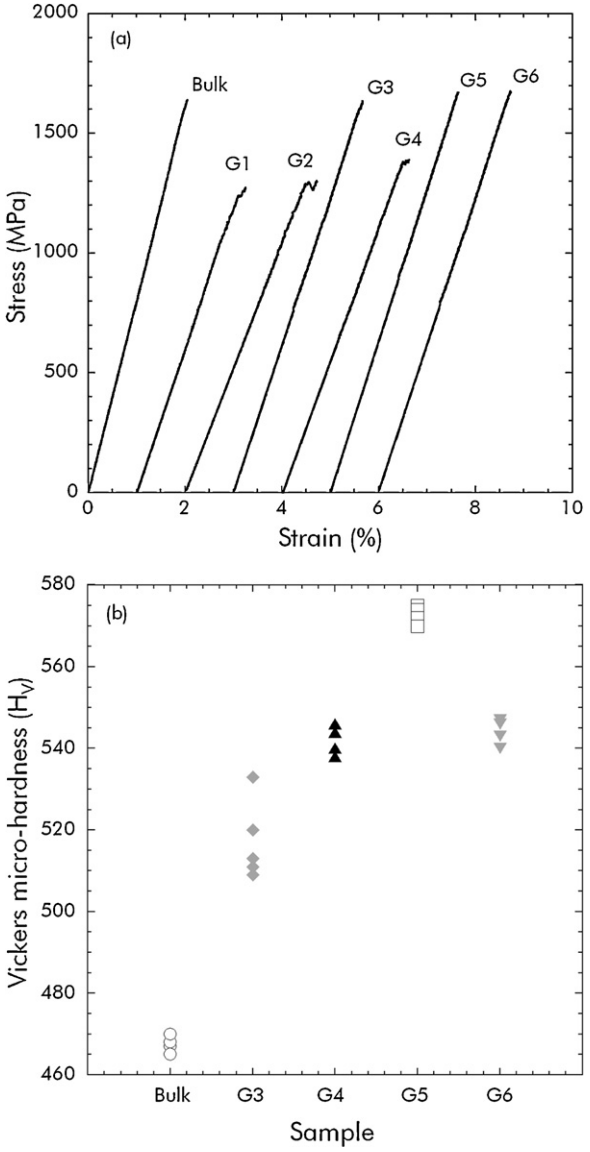

Fig. 5. True stress–true strain compression curves for sintered samples G1–G6, compared to the BMG (a); Vickers micro-hardness at 2000 × *g* for sintered samples G3–G6 (b).

3.3. Behaviour of sintered samples

G3, G5 and G6 exhibit ultimate compressive strengths comparable to BMG monolith prepared by solidification (Fig. 5a) [25]. For those three samples, the Young's modulus is slightly lower than for the BMG, $E > 60$ GPa compared to $E_{BMG} \approx 80$ GPa. G1 and G2 show relatively low compressive strength, which can be explained by the presence of large glass particles and the relatively low level of consolidation, as the raw powder was not sieved and the annealing times were short (3 and 5 min). G1, G2 and G4, which present the lowest compressive strength, also exhibit a slightly different behaviour: fracture is not fragile and a small plateau is noticeable on the compressive curves of those three samples.

In relation to multiple shear bands initiation and deviation at crystalline particles, ductility induced by partial crystallisation in BMGs is generally observed in cast alloys [28]. However, no ductility was observed for SPS samples having the maximum strength. Partial crystallisation in amorphous alloys is also known for increasing hardness [29], which is in good agreement with the data plotted in Fig. 5b, where G5 shows the highest hardness value for an applied load of 2000 g. Hardness of G3, G4 and G6 is about 540 H_V, close to that of a cast monolith BMG and consistent with the ultimate stress value, σ_{max}, measured in compression according the Tabor rule: $\sigma_{max} \approx H_V/3$.

Interestingly, G4 presents the lower ultimate strength and Young's modulus, suggesting that the powder has undergone less consolidation during the sintering process. Lesser particle welding for G4 (compared to G3, which underwent the same annealing time) is attributed to particle size which is about twice larger for G4. Viscous flow is assumed for an amorphous phase in the phenomenology of the initial stage of the sintering process. The consolidation degree, x/D, where x is the neck radius, varies as a function of time (t) and particle size (D) following: $x/D \propto \sqrt{t/D}$. This is in agreement with mechanical investigations indicating that greater consolidation is achieved for samples with small initial particle size. Further consolidation is also obtained if particles are selected to a thin size distribution. The consolidation is thus dependent on the particle size [30]. This can be explained by the higher reactivity of fine powders, in relation to their larger surface curvature. One emphasizes that the sintering rate is modulated by physical properties of the amorphous phase, in particular viscosity. The size effect on consolidation efficiency is well known in conventional sintering. For SPS, the particle size efficiency seemingly holds, but in the particular case of metallic glass powders, it must be balanced with the devitrification amount (as large as the particles are small). A compromise is then necessary in terms of particles size in order to obtain strong sintered glass with limited crystallisation.

Observations of the fracture surfaces, using scanning electron microscopy after compression test, reveal evidence of transgranular shear banding (Fig. 6a) as well as "intergranular" rupture (Fig. 6b). Further analyses of "intergranular" areas show that former particles are rough in the centre and totally smooth at the periphery (Fig. 6c). The centre exhibits a dimple-like structure characteristic of a ductile fracture. Additionally, ductile fracture would mean that free volume is still present in the glass and that micro-shear bandings might be initiated by crystalline particles present underneath. In contrast, origin of the smooth zone is not straightforward. Topology of the rupture surface suggests that the cohesion is not total. It is thus emphasized that the rupture process for sintered samples is radically different compared to quenched monolith, where stress relaxation is localized in few thin shear bands. On one hand, in cast BMGs, the process leads to spontaneous rupture of the specimen into two pieces, due to extended propagation of a single shear band along a shear plane at about 45° off the load axis [25,26]. On the other hand, SPS samples experience early damages which lead to with multiple fragmentation of the sample at the ultimate compression stress.

4. Discussion

According to these results, full densification of MGs through SPS (using pulsed current) seems to be reached during two distinct steps. First, the cohesion between particles is achieved during initial stage of the sintering in the centre of the particle. This first step occurs when necks are still narrow, but leads to a partial cohesion along with a partial devitrification of the MG. However, according to density measurements, total densification is reached. Further densification should happen during a second stage of the sintering process, which occurs when necks are wide enough to allow homogeneous flow of the MG particles and avoid crystallisation in the vicinity of necks. In the following paragraphs, we develop this hypothesis in relation to the sintering driving forces (which can be topological, thermal, but also electrical in the specific case of SPS).

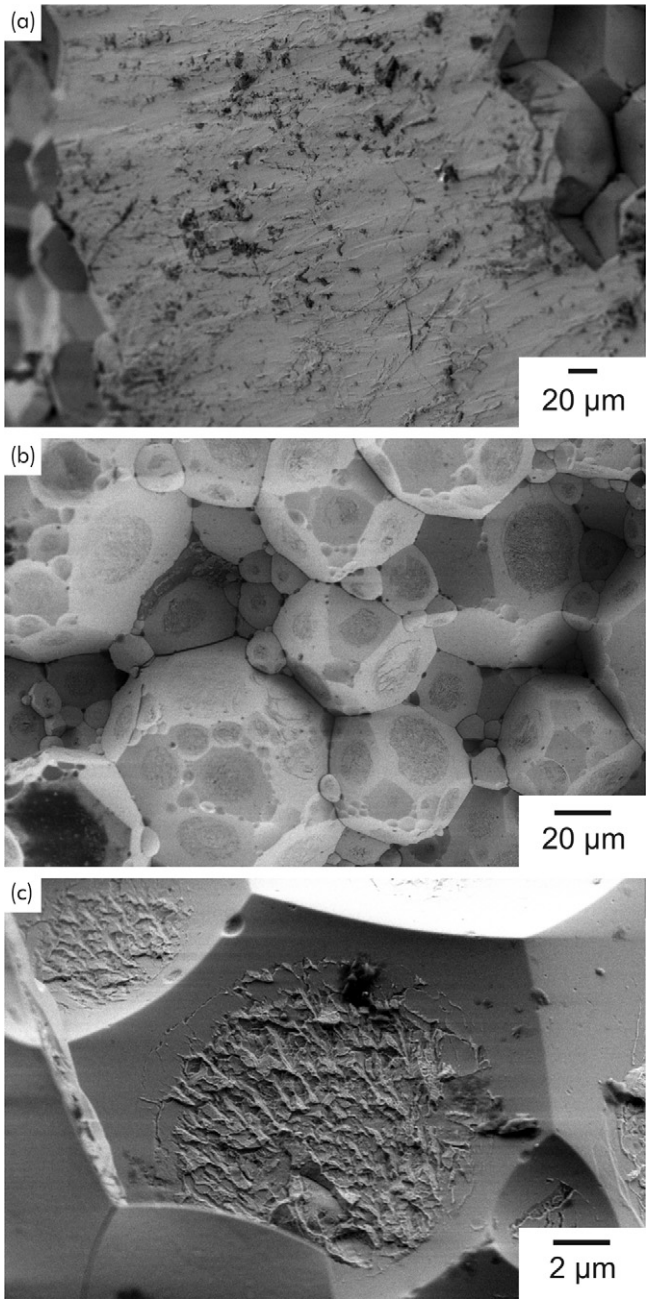

Fig. 6. SEM micrographs showing fracture surfaces of G2, typical of any sintered sample: shear band which propagated trough the particles (a); "intergranular" fracture area, showing the shape of particles after sintering (b); detail of the central area of a particle facet, where a dimple-like rupture is visible (c).

4.1. Assumptions and description of sintering driving forces

Topology of particles in the initial stage of the sintering is a sphere with mean particle radius $R = D/2$, having in average six contact points. The electric current is entering and exiting particles through respectively three contacts (Fig. 7). The current intensity passing through a neck may thus be estimated as: $i_{neck} = \zeta \cdot I(R/\Phi)^2/3$, where $R \sim 35\,\mu m$, the sample radius $\Phi = 5$ mm, and the macroscopic current input is $I = 1200$ A. ζ is the fraction of the macroscopic current passing through the specimen. This parameter is difficult to estimate since it depends on the relative resistance of the powder to die and punches. It also depends on tools geometry, varies with materials resistivity, and changes during the process because of powder density and temperature variations.

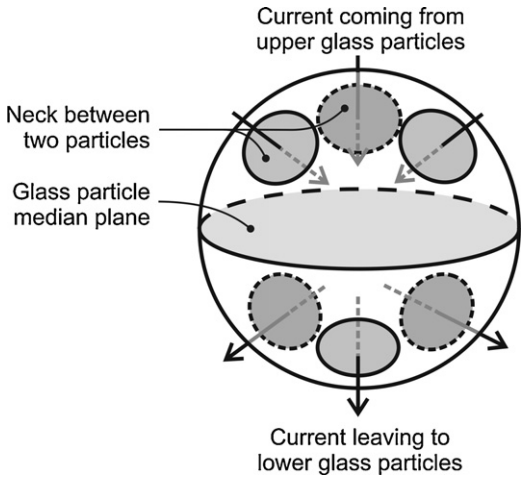

Fig. 7. Repartition of glassy particles at the sintering beginning. Each particle is surrounded by six neighbours, according to compact random close packing. The three upper particles provide electric current to the particle, as the three lower particles drain it, resulting in $i_{neck} = i_{particle}/3$.

When ζ is close to unity, i.e. the resistance of the die is far larger than that of the powder, $i_{neck} \approx 20$ mA.

As shown in Fig. 8a, the neck can furthermore be characterised by its two surface curvature radii, x (concave), which is also the neck radius, and ρ (convex). During the initial stages of sintering, $|\rho| \ll |x|$ and $\rho < 0$ and $x > 0$.

During sintering, both neck growth and devitrification are controlled by diffusional processes. The local atomic flux, J, can be written in a general form:

$$J = -D\frac{\partial c}{\partial z} + \frac{Dc}{kT}(F_c + F_{th} + F_i)$$

where D is the atomic diffusion coefficient, c is the atomic concentration, k is the Boltzmann constant, and T is the temperature.

The mass flow forces are resulting from the neck topology, F_c, the electric potential, F_i, and the thermal gradient, F_{th}. In first approximation, the electric current can be considered as normal to the neck boundary (Fig. 8a). From a two-sphere model, the resulting topological or Laplace force, F_c, is normal to the neck surface (see Fig. 8b). F_c is radial with respect to the neck boundary, as in the usual phenomenology of natural sintering. Consequently, the stress at the neck surface is given by the Laplace law: $\sigma_c \approx \gamma/\rho \approx 2R\gamma/x^2$. Assuming a surface energy $\gamma \approx 2\,J\,m^{-2}$ it should be noticed that σ_c is larger than the applied macroscopic stress (500 MPa) for $x < 500$ nm.

The two other forces, F_i and F_{th} are derived from the electric current passing through the neck. $F_i = qE = Z^* e \rho_e j$, with Z^*, the effective

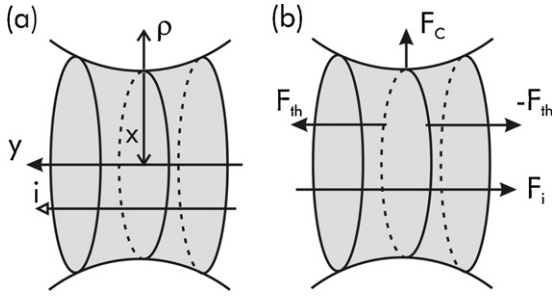

Fig. 8. Outline of a particle neck in the initial stage of the sintering. (a) Topological parameters (ρ, x) are the surface curvature and i is the electric current passing through a neck. The grey zone indicates the heat concentration at the reduced size of the contact point due to Joule dissipation, resulting in temperature gradient in the y and $-y$ directions. (b) Resulting forces from gradients: F_c (topological force, i.e. Laplace force), F_i (electric potential related force) and F_{th} (thermal gradient force).

electric charge of the atom, e, the electron charge, ρ_e, the resistivity and j, the electric current density. F_i is normal to the neck boundary. A thermo-transport force, $F_{th} = -Q/T \times \partial T/\partial y$, with Q the heat of transport, is resulting from the temperature gradient. As detailed below, heat concentration in the vicinity of the neck occurs since the neck size is small compared to the centre of particles size. In this case, much larger electric current density get through the necks. The temperature gradients and the associated force, F_{th}, are normal to the neck boundaries.

From this topology, commonly used in the approach of the classical sintering mechanisms, it results that the Laplace force, F_c (the only one present in natural sintering), should be predominant in the neck growth (sintering degree). The two other forces, F_i and F_{th}, normal to the neck plane (see Fig. 8b), should have minor contributions to the sintering degree, but might be involved in crystalline particles growth along with the concentration gradient ($\partial c/\partial z$) build up during devitrification.

In the following paragraphs, an attempt is made to evaluate the contribution of those forces on sintering and devitrification.

4.2. Thermal state in the vicinity of a neck

The temperature must be large enough to activate diffusion for sintering and particle precipitation and growth. The observation of ZrCu in the MG suggests that during certain stages of the SPS experiments, the temperature can be at least larger than T_x in some parts of the sample. Indeed, even if, in the alloy of interest, ZrCu stability domain should be slightly modified by the presence of other chemical elements, this phase is stable above 1000 K according to the phase diagrams [31]. In contrast, it must be emphasized that the metallic glass is not fully devitrified. This indicates that the balance between temperature increase and heat release by thermal dissipation in the powder leads, in average, to a temperature not too much larger than T_x.

The balance between Joule effect dissipation and heat flow gives the local temperature rate as: $\Delta T/\Delta t \approx (\rho_e j^2)/(\rho_v C_p)$, where ρ_v is the volume weight and C_p is the heat capacity. During an elemental SPS pulse (2 ms on–1 ms off), the current density in the particle is $j_R \approx 3i_{\text{neck}}/(\pi R^2)$ and the resulting temperature increase would be $\Delta T_R \approx 0.08$ K, for $\zeta = 1$ ($\Delta t = 2$ ms, $\rho_v = 6600\ \text{kg m}^{-3}$, $C_p = 420\ \text{J kg}^{-1}\ \text{m}^{-1}$, $\rho_e = 4.4 \times 10^{-7}\ \Omega\,\text{m}$ [32]). This value seems very small, but it is actually largely overestimated (due to various heat and current dissipations). One has to notice that cumulative pulses over about 20 min of experiment would lead to an extremely unrealistic temperature, besides indicating that energy yielding in our particular SPS setting is very poor. Comparatively, the current density in the neck region, $j_{\text{neck}} \approx i_{\text{neck}}/(\pi x^2)$, predicts temperature in the neck region according to $\Delta T_n \approx (\Delta T_R/9) \times (R/x)^4$. It naturally comes that the difference in temperatures between the particle core and the neck region varies as the sintering degree (x/R), and that the power of 4 means that, at small neck sizes, this difference is substantial. The temperature gradient between the neck region and the particle core leads to heat dissipation from these two respective zones, with relaxation time of the order of $\tau \approx R^2/\alpha \approx 0.4$ ms, with the thermal diffusivity, $\alpha = 3.5 \times 10^{-6}\ \text{m}^2\ \text{s}^{-1}$ [32]. τ is smaller than the on (2 ms) and off (1 ms) times of an elemental pulse. It results consequently that during the 2 ms of current on, heat dissipation from the neck to the particle core occurs concomitantly to heat accumulation by Joule effect at the neck. These two concurrent effects have different time and spatial scales. Analytical evaluation of an effective temperature as a function of time at the neck region is thus not allowed. In contrast, due to rapid heat dissipation, homogeneous temperature is rapidly obtained in the overall sample after the off (1 ms) time, which means that the monitoring of temperature by external recording is most likely consistent. Most dramatic is the substantial increase of temperature in the neck region. For example, one may consider a spontaneous event, that is heat accumulation by Joule effect with negligible dissipation, $\Delta t \ll \tau$. Taking $\Delta t \approx \tau/100$, during this spontaneous event, the temperature rises higher than T_x (ΔT starting from room temperature) for neck sizes smaller than 500 nm. This rough evaluation shows that since the very beginning of the sintering, the SPS pulses are able to produce spontaneous temperature increases larger than T_x. The heat is most likely maintained to this range of temperature by cumulative events during the 12 pulses sequence, and then totally dissipated during the 6 ms extra-pauses sequence. One emphasizes that this local temperature increases are not detected by external average measurements, since the pulses frequency is very high and the total volume of neck regions is very small, approximately $(x/R)^4/4$.

4.3. Sintering amount

One of the most reasonable hypotheses is that the rough area observed on the fracture surface (Fig. 6c) is the welded part of the particle. Image processing on fracture surfaces as shown in Fig. 6c estimates the ratio rough area/total surface of a facet (i.e., the sintering amount) at 0.5. If the sintering rate is controlled by viscous flow, it can be described by the relation: $(x/R)^2 = 3\gamma \cdot t/(2\eta \cdot R)$, which estimates $\eta \approx 10^8$ Pa s, for $x/R = 0.5$, $\gamma = 2\ \text{J m}^{-2}$, $t \approx 20$ min. This value of the viscosity is reasonably associated to a temperature in the range of the glass transition for this Zr-based MG, ≈700 K [4], and is also consistent with both the plateau temperature and the total time of our SPS experiments. These calculations thus assess the hypothesis that consolidation is only partial, and achieved in the first moments of the SPS process.

4.4. Devitrification and crystal growth

The crystalline precipitates observed using TEM (Fig. 3) have size of about 50 nm and are separated by about 3–5 times their size, meaning that precipitation rate is low. This structural feature is another evidence that, for the annealing time (about the time of the experiment, 20 min), temperature was not too much larger than T_x. In a precipitation process controlled by the gradient of composition, the growth rate of a spherical particle is described by: $R(t) = [2Dt \times (c_0 - c_i)/(c_p - c_i)]^{1/2}$. The diffusing atom concentrations are respectively c_0 in the glass, c_p in the precipitate, and c_i in the glass at the precipitate interface. Considering the growth of a ZrCu monoclinic precipitate, concentration of Cu in the glass is $c_0 \approx 0.013$ at. Å^{-3}, and the concentration in ZrCu is $c_p \approx 0.030$ at. Å^{-3}. At these values of temperature, the diffusion coefficient, D, is in the range of $10^{-19}\ \text{m}^2\ \text{s}^{-1}$ [33]. Then, the minimum growth time estimated is $t \approx 25$ min, with $c_0 \gg c_i$ and $c_p \gg c_i$ and for the precipitates with $R \approx 25$ nm.

4.5. Influence of thermo- and electro-transport in the precipitate growth

The time for precipitate growth is consistent with the range of the experiment duration. Nevertheless, this remains an estimate since c_i is neglected and D is assumed from literature data. It should be concluded that there is no clear evidence that other mass transport forces (i.e., F_i and F_{th}) are involved in the growth process along with the concentration gradient. Indeed, one may emphasize that thermo-transport is most likely not occurring, since thermal gradients at the necks approximately last only during the 2 ms of current on of the elemental pulses, and there is no diffusive atom displacement during such a short period. For its part, electro-transport may be effective during each pulse. Its potential contribution may be appreciated by comparing atomic fluxes. The flux from concentration gradient is given at the precipitate surface by: $J = D(c_0 - c_i)/R \approx D \times 5.2 \times 10^{-25}$. Electro-transport flux is

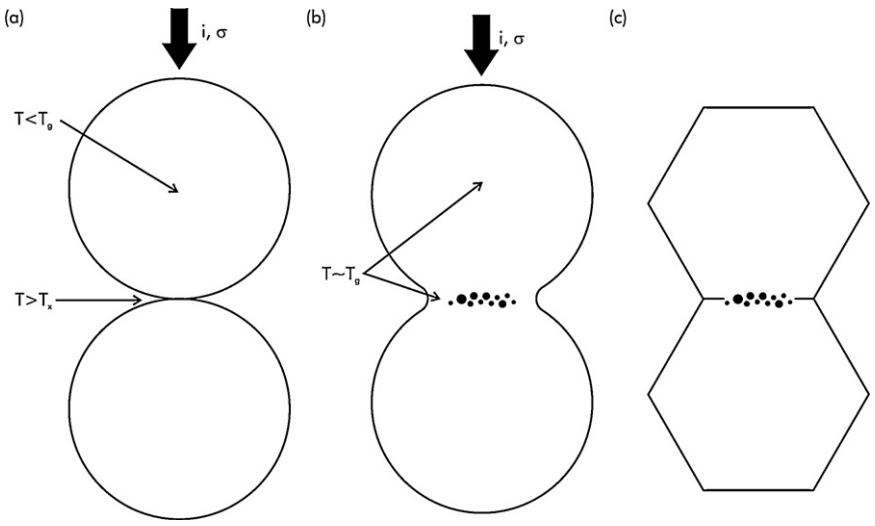

Fig. 9. Schematic representation of the compaction mechanism of MG by SPS: (a) during the early stages of the sintering process, the neck size is very fine, leading to high current densities in their vicinity, and thus to temperatures larger than T_x, responsible for nano-precipitation in those areas; (b) when the neck size is sufficient, all the particle is homogeneously heated, leading to plastic flow; (c) total densification is thus reached.

given by: $J_i = Dc_0Z^*e\rho_e j/kT \approx Dj \times 1.2 \times 10^{-36}$. In order to compete with the concentration gradient, the current density, j, should be larger than $4.3 \times 10^{11}\,A\,m^{-2}$. Those conditions should be effective at neck sizes $x < 120$ nm. Furthermore, it should be concluded that electro-transport is negligible, except during the early stages of the sintering. This result is consistent with electrotransport observed at moderate current density in nano-electronics systems. It has to be emphasized that it is most likely dominant for very fine powder (ultra fine and nanopowders) and might be considered in the phenomenology and modelling of their sintering.

5. Concluding remarks

Spark plasma sintering was used efficiently to produce sintered $Zr_{57}Cu_{20}Al_{10}Ni_8Ti_5$ bulk metallic glass with strength similar to that of the monolith produced by solidification. This processing opens interesting perspectives for the production of multiphase and architectured materials having selected properties. Characterisation of the sintered parts using X-ray diffraction, differential scanning calorimetry, scanning and transmission electron microscopies, revealed elemental features of the micromechanisms involved in the sintering process of the metallic glass and also leading to some extension to metallic powders more generally.

Densification of MGs using SPS might thus be described as follows: heat level generated at initial particles necks is extremely large in the first stage of the sintering when neck is small and its relaxation is very fast due to high thermal diffusivity of metallic alloys. High intensity pulsed current is thus detrimental, and leads to partial devitrification of the metallic glass, formation of high temperature phases and stress gradient by alternate heating and cooling (see Fig. 9a). When necks are wide enough to limit current density, heating becomes homogeneous (Fig. 9b). The amorphous particles can thus flow, leading to a total densification (Fig. 9c).

It must be emphasized that the first stage of sintering is dominant for future properties of the sintered parts. Unfortunately, it cannot be controlled by macroscopic monitoring in SPS (temperature measurements and sintering rate) since these events are localised at necks between particles and represent a negligible volume fraction of the material. Gradual increase of the macroscopic current intensity to moderate current density at the growing particles neck seems the most relevant process to avoid detrimental temperature and stress gradient as well as phase decomposition. This process at the particle scale should be modelled by finite elements method to be controlled.

Regarding the mechanism of SPS sintering, quantitative and qualitative analyses show that according to topological aspects, the sintering is most likely controlled predominantly by the surface tension (Laplace force) as in the natural sintering phenomenology. Electrotransport and thermotransport, occur in a direction normal to the particles neck, and should have some contributions in devitrification, mainly when the neck size is in the nanometer domain.

Acknowledgments

The French MoD is gratefully acknowledged for financial support and continual discussion on the SPS processing. Authors are indebted to H. Couque (Nexter munition) and G. Nicolas (formerly at Cime-Bocuze) and P. Ochin (ICMPE-CNRS) for their interest and fruitful discussions on the subject of sintering and SPS. G. Wang, M.-F. Trichet, B. Villeroy, Y. Cotrebil and J.-L. Bonnentien (ICMPE-CNRS) are acknowledged for assistance in sample preparation and characterisation.

References

[1] A.I. Salimon, M.F. Ashby, Y. Bréchet, A.L. Greer, Materials Science and Engineering A 375–377 (2004) 385–388.
[2] M.F. Ashby, A.L. Greer, Scripta Materialia 54 (2006) 321–326.
[3] C.A. Schuh, T.C. Hufnagel, U. Ramamurty, Acta Materialia 55 (2007) 4067–4109.
[4] A. Inoue, Acta Materialia 48 (2000) 279–306.
[5] W.H. Wang, C. Dong, C.H. Shek, Materials Science and Engineering R 44 (2004) 45–89.
[6] A. Takeuchi, A. Inoue, Materials Transactions 46 (2005) 2817–2829.
[7] W.H Wang, Progress in Materials Science 52 (2007) 540–596.
[8] A.L. Greer, Materials Today 12 (2009) 14–22.
[9] S.A. Miller, R.J. Murphy, Scripta Metallurgica 13 (1979) 673–676.
[10] D.J. Sordelet, E. Rozhkova, P. Huang, P.B. Wheelock, M.F. Besser, M.J. Kramer, M. Calvo-Dahlborg, U. Dahlborg, Journal of Materials Research 17 (2002) 186–198.
[11] Y.B. Kim, H.M. Park, W.Y. Jeung, J.S. Bae, Materials Science and Engineering A 368 (2004) 318–322.
[12] D.J. Sordelet, E. Rozhkova, M.F. Besser, M.J. Kramer, Journal of Non-Crystalline Solids 317 (2003) 137–143.
[13] R. Orrù, R. Licheri, A.M. Locci, A. Cincotti, G. Cao, Materials Science and Engineering R 63 (2009) 127–287.
[14] S. Lee, H. Kato, T. Kubota, A. Makino, A. Inoue, Intermetallics 17 (2009) 218–221.

[15] H. Wang, Y. Liu, X. Pan, C. Feng, F. Ai, Y. Zhang, Journal of Alloys and Compounds 477 (2009) 291–294.
[16] T.S. Kim, J.K. Lee, H.J. Kim, J.C. Bae, Materials Science and Engineering A 402 (2005) 228–233.
[17] J.K. Lee, H.J. Kim, T.S. Kim, S.Y. Shin, Y.C. Kim, J.C. Bae, Journal of Materials Processing Technology 187–188 (2007) 801–804.
[18] P. Dong, W.L. Hou, X.C. Chang, M.X. Quan, J.Q. Wang, Journal of Alloys and Compounds 436 (2007) 118–123.
[19] S.P. Harimkar, S.R. Paital, A. Singh, R. Aalund, N.B. Dahotre, Journal of Non-Crystalline Solids 355 (2009) 2179–2182.
[20] J.K. Lee, H.J. Kim, T.S. Kim, Y.C. Kim, J.C. Bae, Journal of Alloys and Compounds 434–435 (2007) 336–339.
[21] G. Xie, D.V. Louzguine-Luzgin, H. Kimura, A. Inoue, Intermetallics 18 (2010) 851–858.
[22] G. Xie, D.V. Louzguine-Luzgin, L. Song, H. Kimura, A. Inoue, Intermetallics 17 (2009) 512–516.
[23] M. Yamasaki, K. Iwamoto, H. Tamagawa, Y. Kawamura, J.K. Lee, H.J. Kim, J.C. Bae, Materials Science and Engineering A 449–451 (2007) 907–910.
[24] L.Q. Xing, P. Ochin, M. Harmelin, F. Faudot, J. Bigot, J.P. Chevalier, Materials Science and Engineering A 220 (1996) 155–161.
[25] S. Nowak, P. Ochin, A. Pasko, S. Guérin, Y. Champion, Strength of Materials 40 (2008) 154–157.
[26] S. Nowak, P. Ochin, A. Pasko, O. Maciejak, P. Aubert, Y. Champion, Journal of Alloys and Compounds 483 (2009) 139–142.
[27] C.G. MacKamey, D.M. Kroeger, D.S. Easton, J.O. Scarbrough, Journal of Materials Science 121 (1986) 3863–3872.
[28] C. Fan, D. Qiao, T.W. Wilson, H. Choo, P.K. Liaw, Materials Science and Engineering A 431 (2006) 158–165.
[29] S. Gravier, L. Charleux, A. Mussi, J.J. Blandin, P. Donnadieu, M. Verdier, Journal of Alloys and Compounds 434–435 (2007) 79–83.
[30] R.M. German, Powder Metallurgy Science, Metal Powder Industries Federation, Princeton, NJ, USA, 1989.
[31] H. Okamoto, Journal of Phase Equilibria and Diffusion 29 (2008) 204.
[32] M. Yamasaki, S. Kagao, Y. Kawamura, K. Yoshimura, Applied Physics Letters 84 (2004) 4653–4655.
[33] Y. Limoge, Materials Science and Engineering A 226–228 (1997) 228–236.